THE JOURNAL OF PHYSICAL CHEMISTRY LETTERS
A JOURNAL OF THE AMERICAN CHEMICAL SOCIETY

pubs.acs.org/JPCL

Letter

Tailoring Dynamic Charge Response and Trap-State Landscapes with Targeted Phosphine Oxide Additive for Efficient $FAPbBr_3$ Quantum-Dot Light-Emitting Diodes

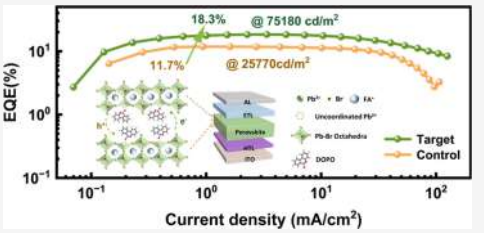
Xinning Wang, Yujie Wen, Di Shen, Maolin Mu, Xiankan Zeng, Chenglong Li, Jianhao Ding, Weiqing Yang, and Wen Li*

Cite This: *J. Phys. Chem. Lett.* 2026, 17, 11242−11251

Read Online

ACCESS | Metrics & More | Article Recommendations | Supporting Information

ABSTRACT: Formamidinium lead bromide ($FAPbBr_3$) perovskite quantum dots (PeQDs) are promising emitters for next-generation displays owing to their narrow emission, high color purity, and solution processability. However, surface-derived trap states promote nonradiative recombination and charge accumulation, limiting PeQLED performance. Here, 9,10-dihydro-9-oxa-10-phosphaphenanthrene-10-oxide is introduced during PeQD synthesis to regulate surface coordination. Spectroscopy supports coordination of its electron-rich P═O group with undercoordinated Pb^{2+} sites, thereby suppressing trap-assisted nonradiative recombination. Reduced Urbach energy and comparative space-charge-limited-current trap-density estimates support lower energetic disorder, while frequency-resolved electrical measurements indicate diminished slow charge relaxation and trap-mediated charge accumulation. Consequently, the optimized PeQLED achieves a peak external quantum efficiency of 18.3%, a maximum luminance of 75,180 cd m^{-2}, and a current efficiency of 85.4 cd A^{-1}. These results link molecular surface coordination with nonradiative-loss suppression and dynamic charge regulation, providing a strategy for efficient PeQLEDs.



Perovskite quantum dots (PeQDs) are promising emitters for next-generation light-emitting diodes because of their tunable band gaps, narrow emission line widths, solution processability, and high photoluminescence quantum yield (PLQY).[1−6] Green and red perovskite light-emitting diodes have reached external quantum efficiencies above 25%, while blue devices continue to advance through composition, dimensionality, and interface engineering.[7−13] Among these materials, formamidinium lead bromide ($FAPbBr_3$) PeQDs are attractive for pure-green emission because they combine high color purity with mild, room-temperature synthesis.[14−18] Their surface coordination, however, is intrinsically dynamic. Ligand loss during purification and film formation can expose undercoordinated Pb sites and increase local structural and energetic disorder.[19−23] The resulting trap-assisted nonradiative recombination, leakage, and charge accumulation limit the fraction of injected carriers that contributes to electroluminescence.

To address the performance limitations of perovskite light-emitting devices, additive engineering has become a widely adopted and effective strategy. Surface-binding molecular multipods, phosphine-oxide-containing ligands, and carboxylic-acid modifiers have been used to stabilize the perovskite lattice or coordinate undercoordinated Pb sites, thereby improving luminescence and device efficiency.[21,24,25] However, many studies primarily correlate chemical passivation with steady-state optical properties or final device metrics, while its relationship with the frequency-dependent electrical response of operating devices remains less explored. A reduced trap density alone does not fully describe device operation, because trap-related polarization and space-charge accumulation may still influence charge utilization and the onset of electroluminescence. Therefore, combining analyses of energetic disorder and trap density with impedance spectroscopy and frequency-dependent capacitance measurements can provide complementary insight into how molecular surface coordination is associated with charge accumulation and relaxation in PeQLEDs.

Here, we introduce 9,10-dihydro-9-oxa-10-phosphaphenanthrene-10-oxide (DOPO) during the synthesis of $FAPbBr_3$ PeQDs to regulate their surface coordination environment. The P═O group provides a Lewis-basic site that is expected to interact with undercoordinated surface Pb sites, whereas the cubic perovskite phase is retained. Optical spectroscopy, Urbach analysis, and comparative SCLC measurements consistently indicate reduced nonradiative loss, energetic

Received: July 27, 2026
Revised: August 26, 2026
Accepted: September 15, 2026
Published: September 18, 2026



Downloaded from pubs.acs.org/jpclcd/article-pdf/17/39/11242/6855931/acs.jpclett.6c02527.pdf by SOUTHWEST JIAOTONG UNIV user on 07 November 2026

© 2026 American Chemical Society

https://doi.org/10.1021/acs.jpclett.6c02527
J. Phys. Chem. Lett. 2026, 17, 11242−11251

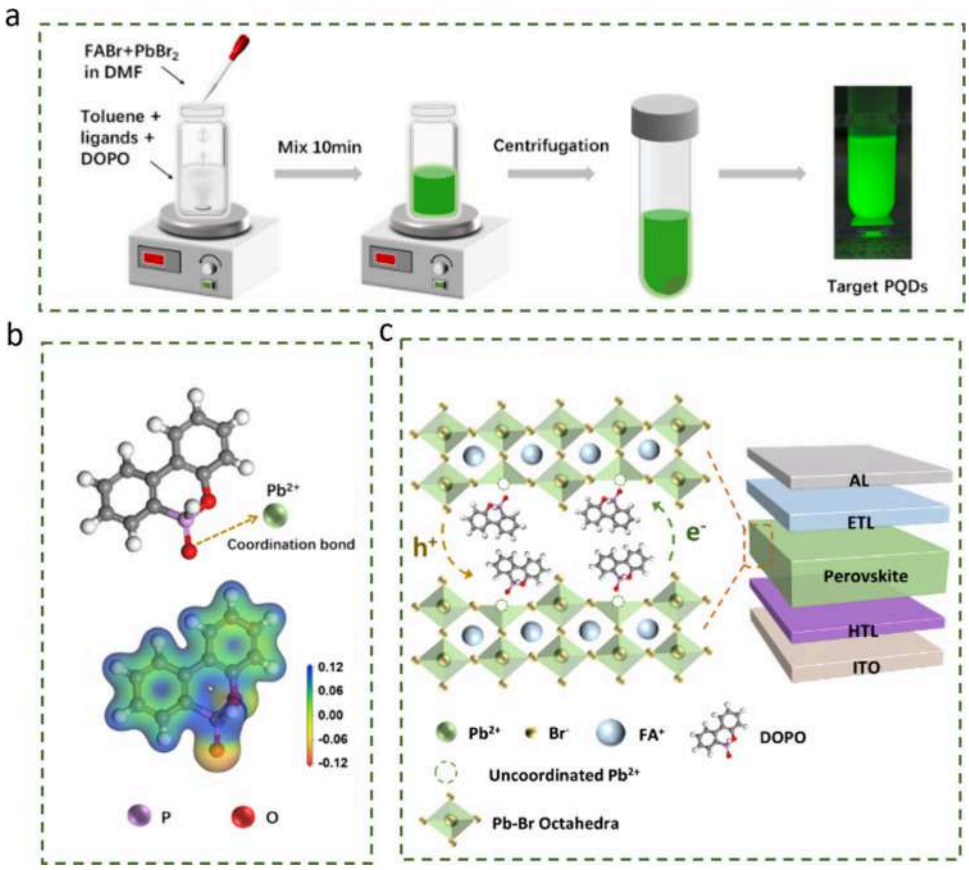


Figure 1. (a) Preparation process of target PeQDs. (b) Chemical structure and electrostatic potential distribution of DOPO. (c) Schematic diagram of DOPO-assisted defect passivation and carrier regulation.

disorder, and electrically active trap density after DOPO incorporation. Frequency-dependent capacitance and impedance measurements further reveal an associated reduction in trap-related charge accumulation and slow charge-relaxation processes. As a result, the device luminance increases from 25,770 cd m^{-2} to 75,180 cd m^{-2}, the current efficiency (CE) from 55.3 cd A^{-1} to 85.4 cd A^{-1}, and the peak external quantum efficiency (EQE) from 11.7% to 18.3%. Overall, the study links molecular surface modification to both the photophysical loss landscape and the dynamic electrical response of PeQLEDs.

$FAPbBr_3$ PeQDs were synthesized by ligand-assisted reprecipitation (LARP), as illustrated in Figure 1a.[26−28] DOPO was dissolved in the antisolvent before precursor injection, and the resulting PeQDs are denoted as the target PeQDs. The chemical structure and calculated electrostatic potential (ESP) distribution of DOPO are shown in Figure 1b and Figure S1. The EPS analysis reveals that the negative electrostatic potential is concentrated around the oxygen atom, identifying the P═O moiety as the most probable Lewis-basic coordination site for undercoordinated Pb^{2+}.[29−32] Accordingly, DOPO is expected to interact with undercoordinated surface Pb sites and modify the local coordination environment of the PeQDs (Figure 1c). Meanwhile, DOPO's fused aromatic skeleton delivers extensive delocalized π-orbitals that overlap with perovskite surface states, lowering interfacial resistance and smoothing carrier transport.[33−35]

The structures and luminescent properties of the control and target PeQDs were compared. Transmission electron microscopy (TEM) revealed that both retained a cubic structure.[25,36] Particle size distribution analysis (Figure 2a,b and Figure S2) indicated a significant decrease in the average particle size of the target PeQDs, from 14.7 nm for the control PeQDs to 12.0 nm. The smaller particle size of DOPO-modified QDs demonstrates that DOPO can serve as an effective surface growth regulator during nanocrystal synthesis. X-ray diffraction (XRD) patterns display the characteristic reflections at 14.8° and 29.8° for both samples (Figure 2c), consistent with the cubic perovskite structure (space group Pm3m).[37,38] No additional crystalline phase or appreciable peak shift is observed, indicating that DOPO does not disrupt the bulk crystal structure. Complementary morphological characterization via scanning electron microscopy (SEM) further reveals notable differences in film quality. Specifically, the surface of the target film is smooth and uniform, whereas the control film exhibits noticeable protrusions and cracks (Figure S3). At the same time, energy-dispersive X-ray spectroscopy (EDS) images reveal a uniform distribution of elements, confirming that DOPO can be successfully blended with perovskite. Atomic force microscopy (AFM) measurements over 5 × 5 μm^2 areas show that the root-mean-square (RMS) roughness decreases from 9.4 nm for the control film to 4.0 nm for the target film (Figure S4), corroborating the formation of a smoother and more spatially uniform emissive layer. Such morphological homogenization can reduce local electric-field concentration and defect-assisted leakage.[26]

The interaction between DOPO and the PeQD surface was examined by X-ray photoelectron spectroscopy (XPS) and Fourier transform infrared (FTIR) spectroscopy. The XPS measurement spectra (Figures S5a-c) showed no detectable P

https://doi.org/10.1021/acs.jpclett.6c02527
J. Phys. Chem. Lett. 2026, 17, 11242−11251

Downloaded from pubs.acs.org/jpclcd/article-pdf/17/39/11242/6855931/acs.jpclett.6c02527.pdf by SOUTHWEST JIAOTONG UNIV user on 07 November 2026

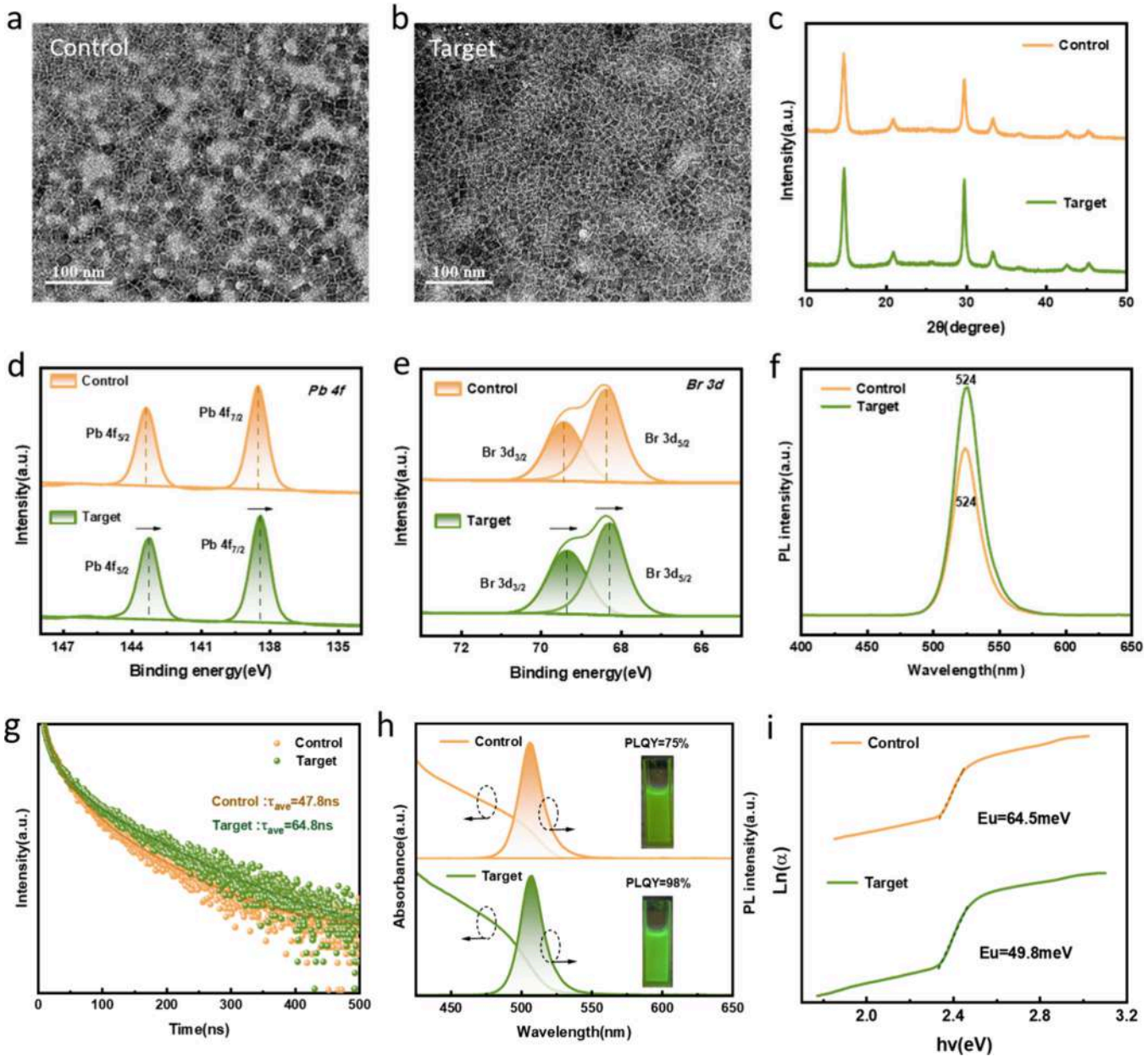


Figure 2. TEM images of (a) control and (b) target PeQDs. (c) XRD patterns of both PeQDs films. XPS spectra of (d) Pb 4f, and (e) Br 3d of both PeQDs films. (f) PL and (g) TRPL spectra of both PeQDs films. (h) UV−vis absorption spectra and the corresponding optical photographs. (i) Urbach energy diagram of both PeQDs films.

signal in the control film, while a significant P 2p signal was observed in the target film. In addition, compared with 8.23% O in the control film, the P content of the target film was 2.71%, and the O content increased by 15.58%. The appearance of phosphorus and the increase in surface oxygen content support the incorporation of DOPO into the target film.[39] In high-resolution spectroscopy, the P 2p double peak of the target film shifts toward lower binding energies relative to pure DOPO (Figure S5d). Meanwhile, after DOPO modification, the Pb 4f and Br 3d peaks also shifted toward lower binding energies (Figure 2d,e). These related changes indicate a redistribution of local electron density and a change in the surface Pb and Br coordination environment after DOPO doping, confirming the strong interaction between Pb^{2+}an Br^{-} ions and the electronegative P═O groups in DOPO. FTIR spectra provides supplementary evidence for this interaction. The target film exhibits additional absorption features related to P═O stretching vibration,[40] which is not present in the control film, indicating that the phosphate functional group remains in the modified PeQDs (Figure S6a). In addition, compared with pure DOPO, the stretching band of P═O underwent significant movement in the DOPO/$PbBr_2$ mixture (Figure S6b). Overall, the results of XPS and FTIR prove that the P═O group forms a coordination bond with the unsaturated Pb^{2+} on the PeQDs surface, rather than simple physical adsorption. To further investigate the effect of additive treatment on the quality of perovskite films, their optical properties were evaluated using steady-state and transient photoluminescence (PL) spectroscopy. Compared with the control group, the PL intensity of the target perovskite films doped with DOPO molecules was significantly enhanced (Figure 2f). As indicated by TEM analysis, both size

https://doi.org/10.1021/acs.jpclett.6c02527
J. Phys. Chem. Lett. 2026, 17, 11242−11251

Downloaded from pubs.acs.org/jpclcd/article-pdf/17/39/11242/6855931/acs.jpclett.6c02527.pdf by SOUTHWEST JIAOTONG UNIV user on 07 November 2026

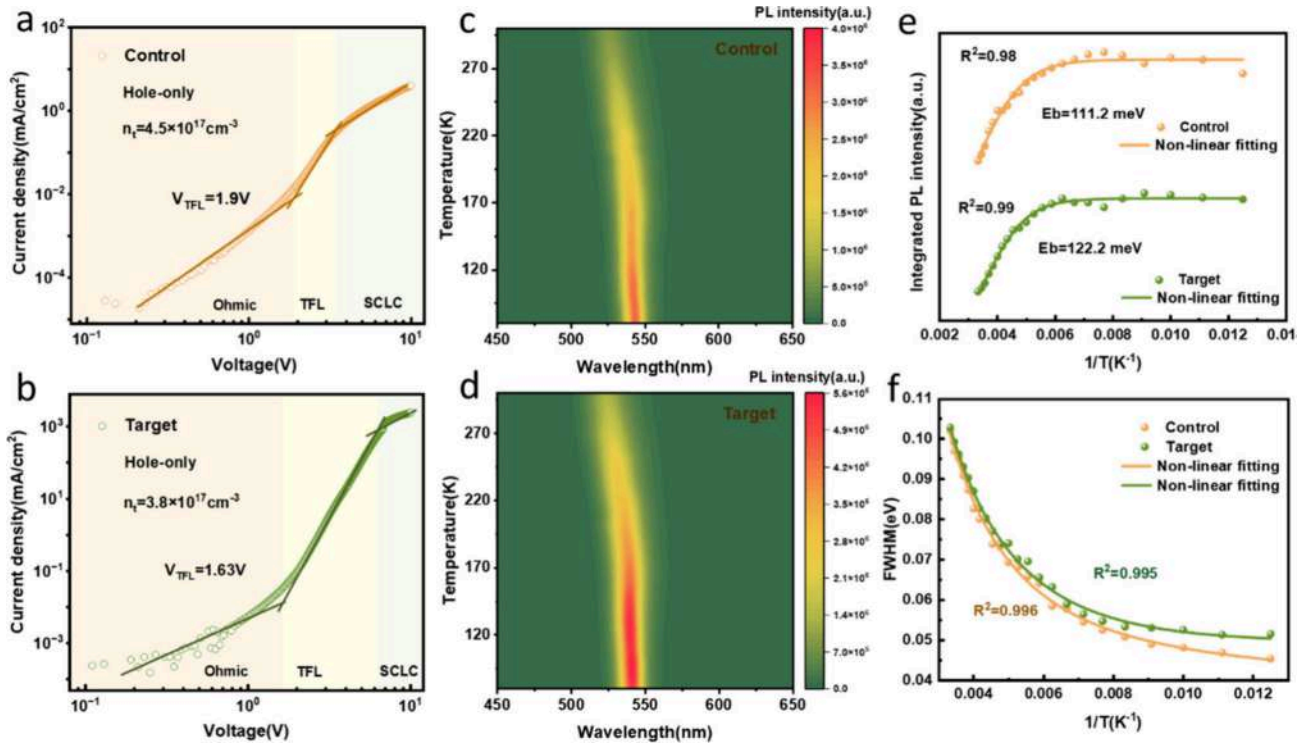


Figure 3. Current density−voltage (J-V) of hole-only devices based on (a) control and (b) target PeQDs films. Temperature-dependent PL spectra of (c) control and (d) target PeQDs films. (e) Integrated PL intensity and (f) fwhm of both PeQDs films.

distributions reside within the weak quantum-confinement regime where prominent confinement-driven spectral shifts are not expected.[21,41] Consequently, the ensemble PL maxima of both samples remain near 524 nm. We then performed time-resolved photoluminescence (TRPL) measurements and fitted the fluorescence decay curves using a triple exponential function $R(t) = A_1\exp(-t/\tau_1) + A_2\exp(-t/\tau_2) + A_3\exp(-t/\tau_3)$,[42] where A_1, A_2 and A_3 are the amplitudes, and τ_1, τ_2 and τ_3 are the time constants for the fast and slow decay lifetimes (Figure 2g and Table S2). The slow decay component is related to radiative recombination, and changes in its parameters provide a direct indication of the intrinsic radiative luminescence capability of the perovskite film. The fitting results show that, following film optimization, the slow decay lifetime τ_3 increased from 93.07 to 113.24 ns, and the proportion of the radiative recombination component A_3 increased significantly. the average fluorescence lifetime of the film increased from 47.77 to 64.79 ns. These results confirm that the optimized perovskite film reduces perovskite trap states and suppresses defect-induced nonradiative recombination and interfacial exciton quenching. Furthermore, by comparing the PL and TRPL spectra of DOPO at different concentrations (Figure S7), 2 mg/mL was determined to be the optimal DOPO concentration.

Figure 2h presents the UV−vis and PL spectra of PeQDs before and after modification; the DOPO-modified target film maintains nearly identical PL maximum and absorption-edge position relative to the control sample yet delivers improved optical density. Accompanied by such spectral features, the absolute PLQY rises from 75% for the control film to 98% for the target film, as summarized in Figure S8. Given that PLQY depends on the relative contributions of radiative (k_r) and nonradiative (k_{nr}) recombination (Table S2),[24,43] the enhanced PLQY, together with extended PL lifetime, confirms effective suppression of nonradiative recombination upon DOPO treatment. The repeated sample analysis (Table S3) showed that non radiative recombination was consistently suppressed after DOPO treatment, thus reducing non radiative losses alleviated trap related exciton quenching and explained the excellent luminescence behavior of the modified PeQD film. To gain a deeper understanding of the enhanced photophysical properties of the target PeQDs, we used UV absorption spectra to fit the Urbach energy (E_U). The E_U is used to quantitatively characterize the band tail states induced by lattice disorder and defects in the material; a lower E_U value indicates fewer defects:[44−46]

$$\alpha(E) = \alpha_0 \exp\left[\sigma(T)\frac{E - E_0}{k_B T}\right]$$

where $\alpha(E)$ is the absorption coefficient; E_0 and α_0 are material parameters; $\sigma(T)$ is the steepness parameter; k_B is the Boltzmann constant; and T is the temperature. As shown in Figure 2i, the E_U decreases from 64.5 meV for the control PeQDs to 49.8 meV for the target PeQDs. Because a smaller E_U corresponds to a sharper absorption edge and a lower density of band-tail states, this result indicates reduced energetic disorder after DOPO incorporation and reduces the overall defect concentration. In conjunction with the above analysis, Urbach's analysis further demonstrates that DOPO molecular coordination alters the landscape of surface-derived trap states without changing the overall crystalline phase.

Using a space-charge limited-current (SCLC) model for hole-type devices, we quantitatively evaluated the defect density in two types of PeQDs films with the following device structure: ITO/PEDOT:PSS/PVK/PeQDs/MoO_3/Ag. Figures 3a and 3b present the current density−voltage (J-V) curves for the two devices, which can be divided into three

https://doi.org/10.1021/acs.jpclett.6c02527
J. Phys. Chem. Lett. 2026, 17, 11242−11251

Downloaded from pubs.acs.org/jpclcd/article-pdf/17/39/11242/6855931/acs.jpclett.6c02527.pdf by SOUTHWEST JIAOTONG UNIV user on 07 November 2026

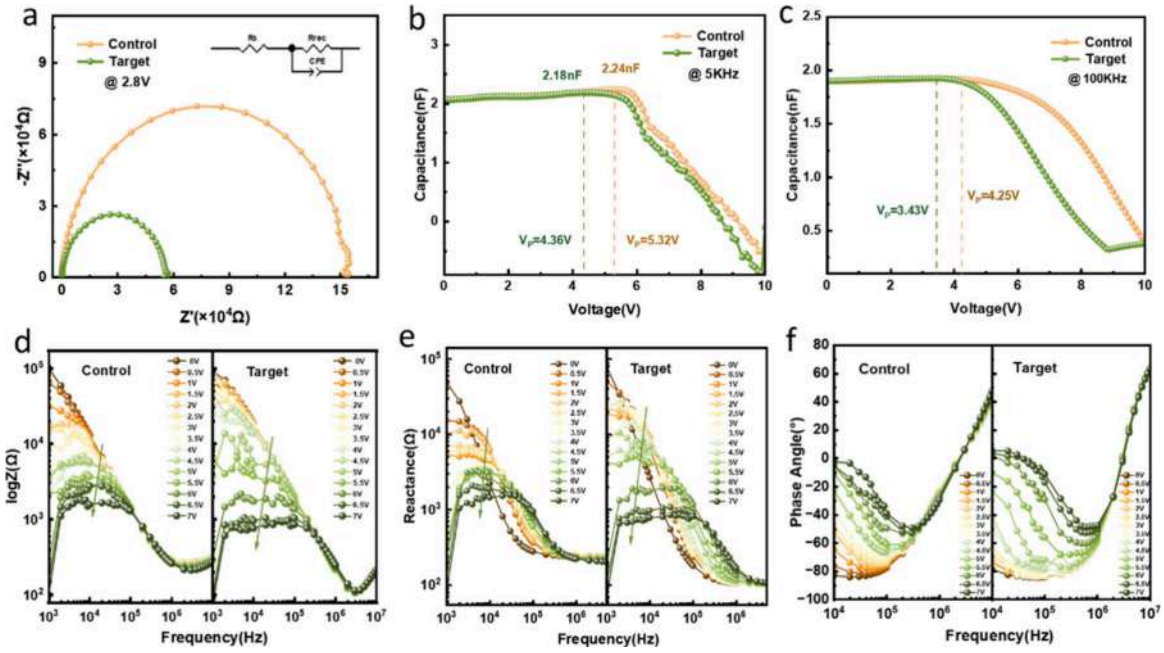


Figure 4. (a) Nyquist plots of impedance spectra. Capacitance−voltage (C−V) plots under (b) low-frequency (f = 5 kHz) and (c) high-frequency (f = 100 kHz). (d-f) Impedance, reactance, and phase angle of both PeQLEDs.

distinct regimes: regions: the ohmic region under low-voltage injection, the trap-filling-limited (TFL) region, and the SCLC region.[47] The trap density can be calculated quantitatively based on the TFL: $n_t = 2\varepsilon\varepsilon 0 V_{TFL}/eL^2$, where e is the elementary charge, ε and $\varepsilon 0$ are the relative permittivity and permittivity of free space of the material, respectively, and L is the thickness of the perovskite emissive layer. Cross-sectional SEM gives L ≈ 80 nm, and the calculation details have been added to Figure S9. The trap-filled limited voltage (V_{TFL}) decreased from 1.90 to 1.63 V, corresponding to a decrease in the estimated trap density from 4.5×10^{17} cm^{-3} to 3.8×10^{17} cm^{-3}. Within this limitation, the lower V_{TFL} of the target film is consistent with the reduced Urbach energy, enhanced PLQY, and prolonged PL lifetime, collectively supporting a decrease in electrically active trap states. In addition, the role of DOPO in modulating the thermal stability and exciton behavior of the film was investigated using temperature-dependent photoluminescence measurements (Figure 3c, d and Figure S10). With increasing temperature, both samples exhibit reduced PL intensity and a blue shift, reflecting thermally activated exciton dissociation and the temperature-dependent lattice response.[43] The exciton binding energy (E_b) of the two PeQDs can be calculated by fitting the temperature-dependent PL integral intensity using the classical Arrhenius model:[48,49]

$$I(T) = \frac{I_0}{1 + Ae^{-E_b/k_BT}}$$

where I_0 is the PL integral intensity at temperature T_0, A is the proportionality constant, k_B is the Boltzmann constant, and E_b represents the energy required for excitons to dissociate into free carriers. As shown in Figure 3e, the fitted E_b value for the control PeQDs after fitting is 111.2 meV, while that for the target PeQDs is 122.2 meV. The larger E_b indicates that excitons in the target film are less susceptible to thermally activated dissociation within the investigated temperature range. The evolution of the temperature-dependent PL full width at half-maximum (fwhm) stems from the scattering of excitons within the film by lattice phonons, which in turn causes spectral broadening. For lead halide perovskites, the temperature dependence of the PL fwhm ($\Gamma(T)$) can be effectively modeled using different scattering mechanisms. The Fröhlich formula is employed for fitting to quantitatively evaluate the charge-phonon coupling strength of perovskite thin films:[48,50]

$$\Gamma(T) = \Gamma_0 + \Gamma_{AC} + \Gamma_{LO} = \Gamma_0 + \gamma_{AC}T + \gamma_{LO}/[e^{(E_{LO}/k_BT)} - 1]$$

Here, Γ_0 denotes the temperature-independent inhomogeneous contribution. The homogeneous broadening components Γ_{AC} and Γ_{LO} correspond to the acoustic (AC) and longitudinal optical (LO) phonon scattering contributions, respectively, where γ_{AC} and γ_{LO} denote the corresponding coupling strengths. E_{LO} represents the LO phonon energy, and k_B is the Boltzmann constant. It is worth noting that the fitted γ_{LO} decreases from 170 to 160 meV after DOPO treatment, while E_{LO} changes from 26.24 to 18.71 meV (Figure 3f and Table S1). This reduction is attributed to DOPO-modified improvements in film quality, resulting the formation of a more compact and spatial homogeneity of film. Meanwhile, the decrease in the LO phonon coupling coefficient γ_{LO} indicates that the target film optimized by DOPO effectively alleviates the charge-phonon coupling within the EML. Combined with the lower Urbach energy and trap density, these results indicate that suppressing surface-induced disorder can reduce defect-related broadening and enhance exciton stability.

Electrochemical impedance spectroscopy was used to connect the modified trap-state landscape with the electrical response of complete PeQLEDs. The Nyquist plots were fitted with the equivalent circuit shown in Figure 4a, comprising a series resistance (Rs) and an effective device resistance (Rrec) coupled with the associated capacitance.[51] Rs reflects the device's interface resistance, while Rrec reflects the internal charge recombination resistance; these can be used to evaluate

https://doi.org/10.1021/acs.jpclett.6c02527
J. Phys. Chem. Lett. 2026, 17, 11242−11251

Downloaded from pubs.acs.org/jpclcd/article-pdf/17/39/11242/6855931/acs.jpclett.6c02527.pdf by SOUTHWEST JIAOTONG UNIV user on 07 November 2026

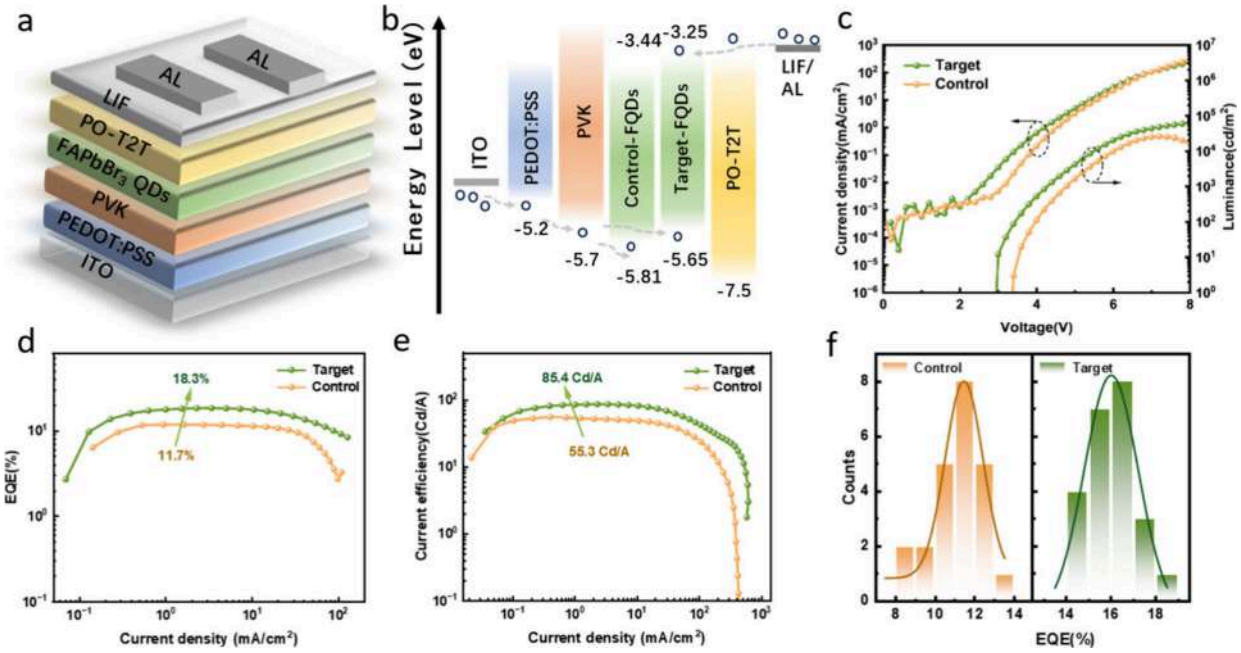


Figure 5. (a) The device structure of PeQLEDs. (b) Energy level diagram of the device structure. (c) Current density−voltage−luminance (J−V−L) curves, (d) EQE−J curves, (e) Current efficiency-current density (CE-J) curves and (f) statistic histogram of EQE based on both PeQLEDs.

the charge injection efficiency and recombination probability in the operating device, respectively. The fitted Rs decreases from 69 to 28 kΩ and the effective parallel resistance from 150 to 56 kΩ after DOPO modification. The evolution of these impedance parameters indicates that the DOPO-modified device suppresses trap-assisted nonradiative carrier loss, thereby enabling a larger proportion of injected carriers to participate in radiative recombination. The decrease in Rrec also indicates that the charge transport characteristics at the device level have been optimized, which jointly contributes to improved carrier injection and radiative recombination efficiencies of the PeQLEDs. Then we evaluated the carrier injection, capture, and recombination kinetics at the

PeQLEDs interface by decoupling the C−V curves at low (5 kHz) and high (100 kHz) frequencies (Figure 4b and 4c). At 5 kHz, the device capacitance initially increases with increasing bias voltage, which can be attributed to enhanced carrier injection, interfacial charge accumulation, and trap-related polarization processes within the emissive layer.[52,53] Upon reaching the characteristic peak voltage (V_P), the charge storage process approaches saturation, and the subsequent decrease in capacitance indicates a transition from charge accumulation-dominated behavior toward more efficient carrier transport and recombination processes. The target PeQLED exhibits V_P of 4.36 V compared with 5.32 V for the control device, indicating facilitated carrier injection and suppressed trap-mediated charge accumulation after DOPO modification. Meanwhile, the slightly reduced diffusion capacitance at V_P (from 2.24 nF to 2.18 nF) suggests decreased charge storage associated with trap states. At 100 kHz, where slow trap responses are suppressed, the earlier capacitance decrease of the target device at 3.43 V reflects accelerated intrinsic charge response and more efficient carrier recombination. Furthermore, the capacitance−voltage−luminance(C−V−L) characteristics provide an additional correlation between electrical response and light emission (Figure S11): the voltage interval between luminance onset and the recombination-dominated region narrows from 1.82 to 1.36 V after DOPO treatment. Collectively, these observations indicate reduced trap-mediated delay and a more rapid conversion of injected charge into emissive states.[54]

Impedance, reactance and phase angle spectra are further used for an in-depth exploration of charge transport kinetics and relaxation behaviors in PeQLEDs from a multiscale electrical perspective. At the low-frequency end of Figure 4d, |Z| at 0 V is approximately 5.8×10^4 Ω for the control device and 6.9×10^4 Ω for the target device. At zero applied bias, appreciable steady-state injection and electroluminescence (EL) are absent; the response therefore reflects the combined dielectric capacitance, effective shunt/leakage resistance, and slow interfacial or trap-related polarization of the multilayer stack rather than a simple carrier-injection resistance.[55,56] The moderately higher zero-bias impedance of the target device is consistent with fewer defect-assisted leakage pathways and a reduced low-frequency trap response after DOPO coordination. Importantly, at 6 V, |Z| decreases to approximately 2.0×10^3 Ω for the control and 1.4×10^3 Ω for the target, demonstrating a stronger bias-induced transition to the conductive operating state in the target device. Meanwhile, the changes in reactance also exhibit a similar trend (Figure 4e), the characteristic relaxation feature shifts toward higher frequency after DOPO treatment, corresponding to a shorter characteristic relaxation time. The voltage-dependent alternating behavior of the resistive and capacitive dominance within the system produces nonmonotonic phase angle variations. As demonstrated in Figure 4f, target devices exhibit significantly larger phase angle shifts with increased voltage compared to their control counterparts. This indicates that the target device exhibits superior interference resilience and diminished susceptibility to electric field trap response, which optimizes the efficiency of carrier recombination. Collectively, these results indicate that DOPO passivation reduces carrier transport barriers and suppresses trap-mediated charge

https://doi.org/10.1021/acs.jpclett.6c02527
J. Phys. Chem. Lett. 2026, 17, 11242−11251

Downloaded from pubs.acs.org/jpclcd/article-pdf/17/39/11242/6855931/acs.jpclett.6c02527.pdf by SOUTHWEST JIAOTONG UNIV user on 07 November 2026

dissipation processes, thereby improving carrier injection and utilization efficiency.

To evaluate the electroluminescent properties of these $FAPbBr_3$ PeQDs, we fabricated PeQLEDs with the following device structure: Glass/ITO/PEDOT:PSS/PVK/PeQDs/PO-T2T/LiF/Al (Figure 5a). As shown in Figure 5b, the conduction band minimum (CBM) and valence band maximum (VBM) of the PeQDs were determined using ultraviolet photoelectron spectroscopy (UPS) and absorption spectroscopy (Figures S12,13), and the corresponding energy level diagrams were constructed. Compared to the reference perovskite layer, DOPO modification optimizes the

surface energy level arrangement of PeQDs films, improving the charge injection balance of the devices. The current density−voltage−luminance (J-V-L) characteristics in Figure 5c show a lower turn-on voltage and higher current density and luminance at the same applied voltage for the target PeQLED. The peak EQE increases from 11.7% to 18.3%, the maximum current efficiency from 55.3 to 85.4 cd A^{-1}, and the maximum luminance from 25,770 to 75,180 cd m^{-2} (Figure 5c-e). Concentration-dependent device characteristics are provided in Figure S14 and identify 2 mg mL^{-1} as the optimum among the investigated DOPO concentrations. Compared to the control PeQLEDs, the DOPO-device exhibits a significant increase in the intensity of the EL peak (Figure S15). To evaluate spectral evolution under increasing electrical stress, EL spectra of the optimized target device were recorded from 4.0 to 8.0 V in 0.5 V increments (Figure S16). The intensity increases strongly with bias, while the emission maximum remains near 524−525 nm and no additional shoulder or secondary emission band emerges. It is worth noting that device aging under continuous constant voltage or constant current driving induces cumulative damage. These degradation pathways can give rise to luminance decay without producing a substantial shift in the EL spectra.[57] The half-life (T_{50}) measurements under constant-voltage operation give approximately 3.1 min for the control and 6.5 min for the target device (Figure S17), confirming the beneficial effect of DOPO passivation on device operational stability. As demonstrated above, DOPO effectively passivates under-coordinated Pb-related static surface traps and suppresses trap-mediated nonradiative recombination, which contributes to the improved initial luminescence efficiency and retarded high-bias EL roll-off. Therefore, such surface passivation primarily eliminates loss channels originating from static traps within the as fabricated QD film, and serves only as one viable strategy toward improved device operational lifetime. Figure 5f shows the EQE histograms for devices; the control devices have an average EQE of 11.2%, while the target devices have an average EQE of 16.6%. Therefore, the excellent electroluminescent performance of the improved device originates from the regulatory effect of DOPO additive. Molecular coordination reduces energy disorder and charge accumulation on the surface, inhibits trap-mediated nonradiative recombination, and enhances carrier utilization efficiency. Simultaneously, it lowers the interfacial charge barrier to balance carrier injection and transport, thereby enhancing the overall photoluminescent output of PeQLEDs.

In summary, this study employed DOPO as a synthetic additive to address the inherent surface trap defects in colloidal $FAPbBr_3$ PeQDs resulting from ligand loss during the purification process. Spectroscopic characterization confirmed that the electron-donating P = O groups of DOPO formed coordination bonds with unsaturated Pb^{2+} sites on the surface, which alleviated lattice energy disorder and suppressed the formation of an electroactive trap landscape. Concurrently, we systematically combined temperature-dependent photoluminescence and multifrequency electrical characterization to elucidate the dynamic charge behavior in operating devices. Combined characterizations reveal that DOPO modification suppresses nonradiative recombination channels, weakens exciton−phonon coupling, and alleviates trap-polarization-induced space-charge accumulation, yielding simultaneous improvements in the luminescence efficiency of quantum-dot films and the electrical performance of resulting devices. Thanks to the improvement of DOPO, the resulting PeQLED achieved significant performance improvements: luminance increased from 25,770 cd m^{-2} to 75,180 cd m^{-2}, current efficiency rose from 55.3 cd A^{-1} to 85.4 cd A^{-1}, and the peak EQE improved from 11.7% to 18.3%. This study reveals the correlation between molecular surface coordination, trap state energetics, and dynamic charge response, and provides new insights into the impact of molecular additives on the performance of PeQLEDs.

EXPERIMENTAL METHODS

Materials

Formamidine bromide (FABr), (1,3,5-triazine2,4,6-triyl)tris(benzene-3,1-diyl)tris(diphenylphosphine oxide) (PO-T2T, 99.9%), poly(9-vinylcarbazole) (PVK), PEDOT:PSS (Clevios Al 4083) and lithium fluoride (LiF, 99.9%) were purchased from Xi'an Polymer Light Technology Co. Ltd. Lead bromide ($PbBr_2$), molybdenum trioxide (MoO_3, 99.95%), decylamine (98%), oleic acid (OA, 90%), and LiF were sourced from Shanghai Aladdin Industrial Corporation Co, Ltd. Keshi provided ethanol, toluene (99.9%), 1-butanol(98%), *n*-octane (98%), *n*-hexane(98%) and N,N-dimethylformamide (DMF, 98%). 9,10-dihydro-9-oxa-10-phosphaphenanthrene-10-oxide (DOPO, 97%) was purchased from Ron Reagent. All chemicals were directly used without further purification.

Preparation of $FAPbBr_3$ QDs

The synthesis of $FAPbBr_3$ QDs was carried out using a modified method based on literature. The $FAPbBr_3$ precursor (150 μL), prepared by dissolving $PbBr_2$ and FABr in DMF with a molar ratio of 1:2.2 and Pb^{2+} concentration at 0.2 M, was injected into a vial containing the antisolvent composed of 5 mL of toluene, 2 mL of 1-butanol, 300 μL of oleic acid, and 25 μL of decylamine, with DOPO predissolved into this antisolvent system as the modification additive. The solution was vigorously stirred for 10 min after the injection, following which it was centrifuged at 13000 rpm for 5 min and the precipitate was collected. The precipitate was dispersed in 1 mL of a mixture of *n*-octane and *n*-hexane with a volume ratio of 2:1. And then centrifuged at 2000 rpm for 2 min. The resulting supernatant was filtered through a 0.22 μm PTFE filter to collect DOPO-modified $FAPbBr_3$ QDs. Prior to the injection of the precursor, the crystallization inducing solution was precooled to 8−10 °C. The room temperature was approximately 28 °C during the experiment.

Fabrication of PeLEDs

The devices were fabricated according to our previous reports. Indium tin oxide (ITO) patterned glass substrates were sequentially cleaned by sonication in deionized optical glass water, acetone, 2-propanol, and ethanol for 15 min each, followed by a 15 min UV−ozone treatment to improve surface wettability. PEDOT:PSS aqueous solution was spin-coated at 4000 rpm for 40 s, and then annealed at 150 °C for 15 min to remove residual solvent. The PEDOT:PSS film was transferred into a nitrogen-filled glovebox and allowed to cool to room temperature. Subsequently, PVK with a concentration of 4 mg/mL was spin-coated in chlorobenzene at 3000 rpm for 30 s. The PVK film was then annealed at 170 °C for 20 min. $FAPbBr_3$ QDs

Downloaded from pubs.acs.org/jpclcd/article-pdf/17/39/11242/6855931/acs.jpclett.6c02527.pdf by SOUTHWEST JIAOTONG UNIV user on 07 November 2026

https://doi.org/10.1021/acs.jpclett.6c02527
J. Phys. Chem. Lett. 2026, 17, 11242−11251

were spin-coated at 1000 rpm for 50 s on the PVK films and then quickly transferred into a high-vacuum evaporator without annealing. Finally, in a low vacuum environment with a pressure of 8×10^{-5} Pa, 40 nm of PO-T2T, 1 nm of LiF, and 100 nm of Al were sequentially deposited. The hole-type device is fabricated by depositing 3 nm of MoO_3 and 80 nm of Ag sequentially on the perovskite film.

Characteristics

Transmission electron microscope (TEM) images were collected on the JEM-2100F instrument at 200 kV. A JEOL JSM-7800 Prime scanning electron microscopy (SEM) with an accelerating voltage of 5 kV was used to characterize the morphologies of the films. The crystalline structure and quality of the $FAPbBr_3$ QD films were investigated by X-ray diffraction (XRD; X'Pert Pro X-ray diffractometer) employing a Cu Kα (λ = 1.5418 Å) at room temperature. X-ray photoelectron spectroscopy (XPS) analysis was performed on a Thermo Scientific ESCALAB 250Xi. The PL spectra, TRPL spectra, and temperature-dependent photoluminescence spectra were investigated by using FLS980. The room-temperature absolute PLQY of the films was measured on Edinburgh-FLS 980 spectrometer by an integrating sphere. The UV absorption spectrum was obtained by a UV-2500 (Shimadzu Corporation). The UPS measurements were conducted by a Thermo ESCALAB 250Xi with a 21.22 eV He I ultraviolet energy. The characterizations of low-frequency (f = 5 kHz) and high-frequency (f = 100 kHz) capacitance−voltage curves of PeQLEDs were performed by a Keithley 4200. The Keithley 2400 source meter combined with a QE-Pro spectrometer (Ocean Optics), was employed to characterize the performances of PeQLEDs in the glovebox.

■ ASSOCIATED CONTENT

Supporting Information

The Supporting Information is available free of charge at https://pubs.acs.org/doi/10.1021/acs.jpclett.6c02527.

Molecular electrostatic potential of DOPO; morphological, elemental, XPS, and FTIR characterization of PeQDs films; optical measurements including PL, TRPL, absolute PLQY, temperature-dependent PL, and UV−vis absorption; cross-sectional device SEM, trap-density calculation, UPS, C−V-L data; QLED device metrics covering EQE-J, J-V-L, bias-dependent EL, and T_{50} lifetime; spectral fitting outputs and statistical photophysical parameters from replicate film samples (PDF)

■ AUTHOR INFORMATION

Corresponding Author

Wen Li − *Key Laboratory of Advanced Technologies of Materials (Ministry of Education), School of Materials Science and Engineering, Southwest Jiaotong University, Chengdu 610031, P. R. China*; orcid.org/0000-0002-2805-3230; Email: liwen3337@swjtu.edu.cn

Authors

Xinning Wang − *Key Laboratory of Advanced Technologies of Materials (Ministry of Education), School of Materials Science and Engineering, Southwest Jiaotong University, Chengdu 610031, P. R. China*

Yujie Wen − *Key Laboratory of Advanced Technologies of Materials (Ministry of Education), School of Materials Science and Engineering, Southwest Jiaotong University, Chengdu 610031, P. R. China*

Di Shen − *Key Laboratory of Advanced Technologies of Materials (Ministry of Education), School of Materials Science and Engineering, Southwest Jiaotong University, Chengdu 610031, P. R. China*

Maolin Mu − *Key Laboratory of Advanced Technologies of Materials (Ministry of Education), School of Materials Science and Engineering, Southwest Jiaotong University, Chengdu 610031, P. R. China*

Xiankan Zeng − *Key Laboratory of Advanced Technologies of Materials (Ministry of Education), School of Materials Science and Engineering, Southwest Jiaotong University, Chengdu 610031, P. R. China*

Chenglong Li − *Key Laboratory of Advanced Technologies of Materials (Ministry of Education), School of Materials Science and Engineering, Southwest Jiaotong University, Chengdu 610031, P. R. China*

Jianhao Ding − *Key Laboratory of Advanced Technologies of Materials (Ministry of Education), School of Materials Science and Engineering, Southwest Jiaotong University, Chengdu 610031, P. R. China*

Weiqing Yang − *Key Laboratory of Advanced Technologies of Materials (Ministry of Education), School of Materials Science and Engineering and Research Institute of Frontier Science, Southwest Jiaotong University, Chengdu 610031, P. R. China*; orcid.org/0000-0001-8828-9862

Complete contact information is available at: https://pubs.acs.org/10.1021/acs.jpclett.6c02527

Notes

The authors declare no competing financial interest.

■ ACKNOWLEDGMENTS

This work was financially supported by the National Key Research and Development Program Young Scientist Project (2023YFB3405700) and National Natural Science Foundation of China (NSFC, grant no. 22509128). The authors would like to thank the Analysis and Testing Center of Southwest Jiaotong University for supporting the XRD and XPS measurements.

■ REFERENCES

(1) Chen, Z.; Li, Z.; Hopper, T. R.; Bakulin, A. A.; Yip, H. L. Materials, Photophysics and Device Engineering of Perovskite Light-Emitting Diodes. *Rep. Prog. Phys.* **2021**, *84* (4), No. 046401.

(2) Veldhuis, S. A.; Boix, P. P.; Yantara, N.; Li, M. J.; Sum, T. C.; Mathews, N.; Mhaisalkar, S. G. Perovskite Materials for Light-Emitting Diodes and Lasers. *Adv. Mater.* **2016**, *28* (32), 6804−6834.

(3) Kim, Y.-H.; Lee, G.-H.; Kim, Y.-T.; Wolf, C.; Yun, H. J.; Kwon, W.; Park, C. G.; Lee, T. W. High Efficiency Perovskite Light-Emitting Diodes of Ligand-Engineered Colloidal Formamidinium Lead Bromide Nanoparticles. *Nano Energy* **2017**, *38*, 51−58.

(4) Stranks, S. D.; Hoye, R. L. Z.; Di, D.; Friend, R. H.; Deschler, F. The Physics of Light Emission in Halide Perovskite Devices. *Adv. Mater.* **2019**, *31* (47), No. e1803336.

(5) Kim, Y. H.; Kim, S.; Kakekhani, A.; Park, J.; Park, J.; Lee, Y. H.; Xu, H. X.; Nagane, S.; Wexler, R. B.; Kim, D. H.; et al. Comprehensive Defect Suppression in Perovskite Nanocrystals for High-Efficiency Light-Emitting Diodes. *Nat. Photonics* **2021**, *15* (2), 148−155.

(6) Fakharuddin, A.; Gangishetty, M. K.; Abdi-Jalebi, M.; Chin, S.-H.; bin Mohd Yusoff, A. R.; Congreve, D. N.; Tress, W.; Deschler, F.; Vasilopoulou, M.; Bolink, H. J. Perovskite Light-Emitting Diodes. *Nat. Electron.* **2022**, *5* (4), 203−216.

(7) Chu, Z.; Ye, Q.; Zhao, Y.; Ma, F.; Yin, Z.; Zhang, X.; You, J. Perovskite Light-Emitting Diodes with External Quantum Efficiency

Downloaded from pubs.acs.org/jpclcd/article-pdf/17/39/11242/6859831/acs.jpclett.6c02527.pdf by SOUTHWEST JIAOTONG UNIV user on 07 November 2026

Exceeding 22% via Small-Molecule Passivation. *Adv. Mater.* **2021**, *33* (18), No. e2007169.
(8) Bai, W.; Xuan, T.; Zhao, H.; Dong, H.; Cheng, X.; Wang, L.; Xie, R. J. Perovskite Light-Emitting Diodes with an External Quantum Efficiency Exceeding 30%. *Adv. Mater.* **2023**, *35* (39), No. e2302283.
(9) Jang, K. Y.; Hwang, S. Y.; Woo, S. J.; Yoon, E.; Park, C. Y.; Kim, S. Y.; Kim, D. H.; Kim, H.; Park, J.; Sargent, E. H.; et al. Efficient Deep-Blue Light-Emitting Diodes through Decoupling of Colloidal Perovskite Quantum Dots. *Adv. Mater.* **2024**, *36* (39), No. e2404856.
(10) Ye, L.; Gao, Y.; Feng, Y.; Zhu, X.; Ma, Z.; Zhang, D.; He, Y.; He, H.; Ye, Z.; Dai, X. Suppressing Interlayer Ion Migration in $CsPbX_3$ Nanocrystal Films for Realizing Efficient and Stable Electroluminescence. *Adv. Mater.* **2025**, *37* (33), No. e2505214.
(11) Zheng, S.; Wang, Z. B.; Jiang, N. Z.; Huang, H. L.; Wu, X. M.; Li, D.; Teng, Q.; Li, J. Y.; Li, C. H.; Li, J. S.; et al. Ultralow Voltage-Driven Efficient and Stable Perovskite Light-Emitting Diodes. *Sci. Adv.* **2024**, *10* (36), eadp8473.
(12) Ren, H.; Wang, S.; Nong, Y.; Sun, Y.; Wang, J.; Li, M.; Xu, L.; Yao, J.; Song, J. 22.8%-EQE and Ns-Level Response $CsPbBr_3$ Perovskite Quantum Dot-Based Light-Emitting Diodes. *Adv. Funct. Mater.* **2026**, *36* (40), No. e29207.
(13) Zhang, X.; Yin, J.; Chen, Y.; Zhu, X.; Lu, W.; Guo, Z.; Yang, C.; Zhang, H. Efficient Red Quantum Dot Light-Emitting Diodes Realized by PEDOT:PSS-Free Ternary Blended Hole-Transport Layers with a Lowered Energy Barrier and Suppressed Leakage. *ACS Appl. Energy Mater.* **2026**, *9* (7), 4075−4083.
(14) Zhang, C. X.; Wang, S.; Li, X. M.; Yuan, M. J.; Turyanska, L.; Yang, X. Y. Core/Shell Perovskite Nanocrystals: Synthesis of Highly Efficient and Environmentally Stable $FAPbBr_3/CsPbBr_3$ for LED Applications. *Adv. Funct. Mater.* **2020**, *30* (31), No. e1910582.
(15) Bhatia, H.; Ghosh, B.; Debroye, E. Colloidal $FAPbBr_3$ Perovskite Nanocrystals for Light Emission: What's Going On? *J. Mater. Chem. C* **2022**, *10* (37), 13437−13461.
(16) Kim, J. S.; Heo, J. M.; Park, G. S.; Woo, S. J.; Cho, C.; Yun, H. J.; Kim, D. H.; Park, J.; Lee, S. C.; Park, S. H.; et al. Ultra-Bright, Efficient and Stable Perovskite Light-Emitting Diodes. *Nature* **2022**, *611* (7937), 688−694.
(17) Zhao, H.; Chen, H.; Bai, S.; Kuang, C.; Luo, X.; Teng, P.; Yin, C.; Zeng, P.; Hou, L.; Yang, Y.; et al. High-Brightness Perovskite Light-Emitting Diodes Based on $FAPbBr_3$ Nanocrystals with Rationally Designed Aromatic Ligands. *ACS Energy Lett.* **2021**, *6* (7), 2395−2403.
(18) Patra, A.; Bera, S.; Nasipuri, D.; Dutta, S. K.; Pradhan, N. Tuning Facets and Controlling Monodispersity in Organic−Inorganic Hybrid Perovskite $FAPbBr_3$ Nanocrystals. *ACS Energy Lett.* **2021**, *6* (8), 2682−2689.
(19) Li, J. H.; Xu, L. M.; Wang, T.; Song, J. Z.; Chen, J. W.; Xue, J.; Dong, Y. H.; Cai, B.; Shan, Q. S.; Han, B. N.; et al. 50-Fold EQE Improvement up to 6.27% of Solution-Processed All-Inorganic Perovskite $CsPbBr_3$ QLEDs via Surface Ligand Density Control. *Adv. Mater.* **2017**, *29* (5), No. e1603885.
(20) Wang, J.; Li, M.; Fan, W.; Xu, L.; Yao, J.; Wang, S.; Song, J. Ligand Compensation Enabling Efficient and Stable Exciton Recombination in Perovskite QDs for High-Performance QLEDs. *Appl. Phys. Rev.* **2024**, *11* (3), No. 031405.
(21) Luo, Y.; Wang, S.; Li, W.; Cao, X.; Zhang, C.; Dai, J.; Wang, L.; Yang, X. Dual Ligand Strategy to Manipulate Growth Kinetics of $FAPbBr_3$ Nanocrystals for High-Performance Light-Emitting Diodes. *Small Methods* **2025**, *9* (10), No. e2401694.
(22) Bai, Y.; Hao, M.; Ding, S.; Chen, P.; Wang, L. Surface Chemistry Engineering of Perovskite Quantum Dots: Strategies, Applications, and Perspectives. *Adv. Mater.* **2022**, *34* (4), No. e2105958.
(23) Lee, J.-S.; Lee, S.; Kim, H.; Yu, W.; Lee, H.; Jang, J.; Lee, S.; Park, E.; Ahn, H.; Hong, S.; et al. Highly Bright Deep-Blue Perovskite Light-Emitting Diodes via Dual-Passivating Additive-Based Synergetic Solid-State Halide Exchange. *Adv. Opt. Mater.* **2026**, *14* (14), No. e03811.
(24) Kim, D. H.; Woo, S. J.; Huelmo, C. P.; Park, M. H.; Schankler, A. M.; Dai, Z. B.; Heo, J. M.; Kim, S.; Reuveni, G.; Kang, S. S.; et al. Surface-Binding Molecular Multipods Strengthen the Halide Perovskite Lattice and Boost Luminescence. *Nat. Commun.* **2024**, *15* (1), 12.
(25) Zhang, J. B.; Zhang, D. D.; Zhou, X.; Lian, L. Y.; Shen, C.; Su, C. H.; Fang, S. Y.; Liang, X. F.; Yuan, F. L.; Hou, L. T.; et al. In-Situ Surface Repair of $FAPbBr_3$ Quantum Dots toward High-Performance Pure-Green Perovskite Light-Emitting Diodes. *Nano Lett.* **2024**, *24* (39), 12196−12203.
(26) Chen, Y.; Zeng, X.; Yan, C.; Yang, S.; Pan, L.; Li, C.; Mu, M.; Li, W.; Tang, G.; Yang, W. Suppressing Leakage Current and Charge Accumulation via Perovskite Interface Morphology Regulation for Efficient Light-Emitting Diodes. *Chem. Eng. J.* **2024**, *495*, 153520.
(27) Chen, Y.; Yan, C.; Chen, Z.; Zeng, X.; Wang, Q.; Yang, S.; Pan, L.; Li, C.; Mu, M.; Li, W.; et al. Interfacial Coulomb-Enhanced Charge Injection for Efficient Perovskite Light-Emitting Diodes. *Mater. Today Phys.* **2024**, *43*, 101413.
(28) Pan, L.; Zeng, X.; Qu, Y.; Mu, M.; Yang, S.; Chen, Y.; Li, C.; Dai, L.; Tao, L.; Xin, H.; et al. Bidirectional Inhibiting Interfacial Ion Migration in the Inorganic Hole Transport Layer for Perovskite Light-Emitting Diodes. *Small* **2024**, *20* (48), No. e2405528.
(29) Li, C.; Zeng, X.; Pan, L.; Chen, Y.; Mu, M.; Shen, D.; Wang, X.; Yang, W.; Li, W. Hexamethylene Diisocyanate-Modulated Mixed-Halide Perovskite Enables Efficient and Stable Blue Light-Emitting Diodes. *ACS Appl. Mater. Interfaces* **2025**, *17* (39), 55045−55053.
(30) Li, Y. H.; Xia, Y.; Chen, C. H.; Jin, R. J.; Nar, A.; Chen, J.; Li, N.; Wang, K. L.; Yavuz, I.; Wang, Z. K. Surficial Homogenic Effect Enables Highly Stable Deep-Blue Perovskite Light-Emitting Diodes. *Angew. Chem., Int. Ed. Engl.* **2024**, *63* (46), No. e202412915.
(31) Liu, H. P.; Li, T. R.; Wang, Y. H. 2-Bromohexadecanoic Acid as a Novel Bidentate Ligand for Passivation of Cesium Lead Halide Perovskite Nanocrystals with near-Unity Photoluminescence Quantum Yield and Superior Photostability. *ACS Appl. Mater. Interfaces.* **2025**, *17* (16), 24146−24156.
(32) Xia, Z.; Jiang, J.; Wang, A.; An, D.; Li, Z.; Zheng, H.; Yin, Z.; He, G.; You, J.; Zhang, X. Overall Performance Improvement of Perovskite Green LEDs by $CsPbBr_3$&Cs_4PbBr_6 Nanocrystals and Molecular Doping. *Adv. Mater.* **2025**, *37* (34), No. e2506187.
(33) Li, W.; Lai, X.; Meng, F.; Li, G.; Wang, K.; Kyaw, A. K. K.; Sun, X. W. Efficient Defect-Passivation and Charge-Transfer with Interfacial Organophosphorus Ligand Modification for Enhanced Performance of Perovskite Solar Cells. *Sol. Energy Mater. Sol. Cells* **2020**, *211*, 110527.
(34) Zhao, C.; Wu, W.; Zhan, H.; Yuan, W.; Li, H.; Zhang, D.; Wang, D.; Cheng, Y.; Shao, S.; Qin, C.; et al. Phosphonate/Phosphine Oxide Dyad Additive for Efficient Perovskite Light-Emitting Diodes. *Angew. Chem., Int. Ed.* **2022**, *61* (13), No. e202117374.
(35) Zhao, Y.; Li, M.; Qin, X.; Yang, P.; Zhang, W.-H.; Wei, Z. Efficient Perovskite Light-Emitting Diodes by Buried Interface Modification with Triphenylphosphine Oxide. *ACS Appl. Mater. Interfaces.* **2023**, *15* (2), 3644−3650.
(36) Wang, Y.; Wang, S.; Li, R.; Li, W.; Long, T.; Wang, L.; Kong, L.; Cao, F.; Wu, Q.; Jia, G.; et al. Quantum-Confined Perovskite Nanocrystals Enabled by Negative Catalyst Strategy for Efficient Light-Emitting Diodes. *Small* **2024**, *20* (44), No. e2402825.
(37) Slimi, B.; Mollar, M.; Ben Assaker, I.; Kriaa, A.; Chtourou, R.; Marí, B. Synthesis and Characterization of Perovskite $FAPbBr_{3-x}I_x$ Thin Films for Solar Cells. *Monatsh. fur Chem.* **2017**, *148* (5), 835−844.
(38) Protesescu, L.; Yakunin, S.; Bodnarchuk, M. I.; Krieg, F.; Caputo, R.; Hendon, C. H.; Yang, R. X.; Walsh, A.; Kovalenko, M. V. Nanocrystals of Cesium Lead Halide Perovskites ($CsPbX_3$, X = Cl, Br, and I): Novel Optoelectronic Materials Showing Bright Emission with Wide Color Gamut. *Nano Lett.* **2015**, *15* (6), 3692−3696.
(39) Ali, W.; Zilke, O.; Danielsiek, D.; Salma, A.; Assfour, B.; Shabani, V.; Caglar, S.; Phan, H. M.; Kamps, L.; Wallmeier, R.; et al. Flame-Retardant Finishing of Cotton Fabrics Using Dopo Function-

Downloaded from pubs.acs.org/jpclcd/article-pdf/17/39/11242/6855931/acs.jpclett.6c02527.pdf by SOUTHWEST JIAOTONG UNIV user on 07 November 2026

https://doi.org/10.1021/acs.jpclett.6c02527
J. Phys. Chem. Lett. 2026, 17, 11242−11251

alized Alkoxy- and Amido Alkoxysilane. *Cellulose* **2023**, *30* (4), 2627−2652.
(40) Peng, W.; Xu, Y. X.; Nie, S. B.; Yang, W. A Bio-Based Phosphaphenanthrene-Containing Derivative Modified Epoxy Thermosets with Good Flame Retardancy, High Mechanical Properties and Transparency. *RSC Adv.* **2021**, *11* (49), 30943−30954.
(41) Cui, J.; Beyler, A. P.; Coropceanu, I.; Cleary, L.; Avila, T. R.; Chen, Y.; Cordero, J. M.; Heathcote, S. L.; Harris, D. K.; Chen, O.; et al. Evolution of the Single-Nanocrystal Photoluminescence Linewidth with Size and Shell: Implications for Exciton−Phonon Coupling and the Optimization of Spectral Linewidths. *Nano Lett.* **2016**, *16* (1), 289−296.
(42) Wang, Q.; Chen, Y.; Yan, C.; Zeng, X.; Fu, X.; Pan, L.; Cao, J.; Yang, S.; Li, W.; Chen, X.; et al. Molecularly Designing a Passivation ETL to Suppress EQE Roll-off of PeLEDs. *ACS Energy Lett.* **2023**, *8* (9), 3710−3719.
(43) Mu, M.; Li, W.; Pan, L.; Zeng, X.; Wang, Q.; Chen, Y.; Li, C.; Shen, D.; Wang, X.; Yang, S.; et al. Interface Bridge Engineering for High Efficient Hole Injection in CZTS-Based Perovskite Light-Emitting Diodes. *Adv. Opt. Mater.* **2025**, *13* (27), No. e01028.
(44) Zhang, C.; Mahadevan, S.; Yuan, J.; Ho, J. K. W.; Gao, Y.; Liu, W.; Zhong, H.; Yan, H.; Zou, Y.; Tsang, S.-W.; et al. Unraveling Urbach Tail Effects in High-Performance Organic Photovoltaics: Dynamic vs Static Disorder. *ACS Energy Lett.* **2022**, *7* (6), 1971−1979.
(45) Hu, L.; Duan, L.; Yao, Y.; Chen, W.; Zhou, Z.; Cazorla, C.; Lin, C.-H.; Guan, X.; Geng, X.; Wang, F.; et al. Quantum Dot Passivation of Halide Perovskite Films with Reduced Defects, Suppressed Phase Segregation, and Enhanced Stability. *Adv. Sci.* **2022**, *9* (2), No. e2102258.
(46) Caselli, V. M.; Wei, Z.; Ackermans, M. M.; Hutter, E. M.; Ehrler, B.; Savenije, T. J. Charge Carrier Dynamics upon Sub-Bandgap Excitation in Methylammonium Lead Iodide Thin Films: Effects of Urbach Tail, Deep Defects, and Two-Photon Absorption. *ACS Energy Lett.* **2020**, *5* (12), 3821−3827.
(47) Le Corre, V. M. Space-Charge-Limited Current Measurements: A Problematic Technique for Metal Halide Perovskites. *J. Phys. Chem. Lett.* **2024**, *15* (39), 10001−10008.
(48) Ai, B.; Liu, C.; Deng, Z.; Wang, J.; Han, J.; Zhao, X. Low Temperature Photoluminescence Properties of $CsPbBr_3$ Quantum Dots Embedded in Glasses. *Phys. Chem. Chem. Phys.* **2017**, *19* (26), 17349−17355.
(49) Wei, K.; Cui, M.; Hu, C.; Wei, S.; Zhang, Z.; Zhou, T.; Zhang, J.; Yue, X.; Yin, K.; Sun, C.; et al. Managing Edge States in Reduced-Dimensional Perovskites for Highly Efficient Deep-Blue LEDs. *Adv. Mater.* **2025**, *37* (25), No. e2412041.
(50) Zeng, X.; Yan, C.; Wang, Q.; Cao, J.; Fu, X.; Yang, S.; Chen, Y.; Pan, L.; Li, W.; Yang, W. High Curvature PEDOT:PSS Transport Layer toward Enhanced Perovskite Light-Emitting Diodes. *Small* **2023**, *19* (47), No. e2304411.
(51) Zeng, X.; Yin, Q.; Pan, L.; Chen, Y.; Li, C.; Mu, M.; Wang, Q.; Li, W.; Yang, W. Hole Delayed-Release Effect of Inorganic Interfacial Dipole Layer on Charge Balance for Boosting $CsCu_2I_3$ Light-Emitting Diodes. *ACS Nano* **2025**, *19* (12), 11878−11890.
(52) Xiao, X.; Ye, T.; Sun, J.; Qu, X.; Ren, Z.; Wu, D.; Ding, S.; Sun, X. W.; Choy, W. C. H.; Wang, K. Capacitance−Voltage Characteristics of Perovskite Light-Emitting Diodes: Modeling and Implementing on the Analysis of Carrier Behaviors. *Appl. Phys. Lett.* **2022**, *120* (24), 243501.
(53) Xu, L.; Liu, G.; Xiang, H.; Wang, R.; Shan, Q.; Yuan, S.; Cai, B.; Li, Z.; Li, W.; Zhang, S.; et al. Charge-Carrier Dynamics and Regulation Strategies in Perovskite Light-Emitting Diodes: From Materials to Devices. *Appl. Phys. Rev.* **2022**, *9* (2), No. 021308.
(54) Loganathan, A.; Do, T.-H.; Fu, Y.-S.; Guo, T.-F. From Traps to Transport: Modulating Interfacial Carrier Dynamics in Perovskite LEDs by Additive Passivation. *J. Phys. Chem. C* **2026**, *130* (2), 1105−1113.
(55) Futscher, M. H.; Gangishetty, M. K.; Congreve, D. N.; Ehrler, B. Quantifying Mobile Ions and Electronic Defects in Perovskite-Based Devices with Temperature-Dependent Capacitance Measurements: Frequency vs Time Domain. *J. Chem. Phys.* **2020**, *152* (4), No. 044202.
(56) Xiao, H.; Wang, K.; Wang, R.; Chen, W.; Chiang, K. S. Equivalent Circuit of Quantum-Dot LED and Acquisition of Carrier Lifetime in Active Layer. *IEEE Electron Device Lett.* **2020**, *41* (1), 87−90.
(57) Lee, H.; Ko, D.; Lee, C. Direct Evidence of Ion-Migration-Induced Degradation of Ultrabright Perovskite Light-Emitting Diodes. *ACS Appl. Mater. Interfaces.* **2019**, *11* (12), 11667−11673.

Downloaded from pubs.acs.org/jpclcd/article-pdf/17/39/11242/6855931/acs.jpclett.6c02527.pdf by SOUTHWEST JIAOTONG UNIV user on 07 November 2026

https://doi.org/10.1021/acs.jpclett.6c02527
J. Phys. Chem. Lett. 2026, 17, 11242−11251